Linear diattenuation imaging of biological tissues with near infrared Mueller scanning microscopy

MATTHIEU DUBREUIL,[1,3,*] ⓘ FLORINE TISSIER,[2] SYLVAIN RIVET,[1,3] AND YANN LE GRAND[1]

[1]*Université de Bretagne Occidentale, Laboratoire d'Optique et de Magnétisme OPTIMAG EA 938, IBSAM, 6 Avenue Le Gorgeu, Brest 29238, France*
[2]*Université de Bretagne Occidentale, Laboratoire Optimisation des Régulations Physiologiques ORPHY EA 4324, IBSAM, 6 Avenue Le Gorgeu, Brest 29238, France*
[3]*These authors contributed equally to this work*
*matthieu.dubreuil@univ-brest.fr

Abstract: Among the multitude of optical polarization contrasts that can be observed in complex biological specimens, linear diattenuation (LD) imaging has received little attention. It is indeed challenging to image LD with basic polarizing microscopes because it is often relatively small in comparison with linear retardance (LR). In addition, interpretation of LD images is not straightforward when experiments are conducted in the visible range because LD can be produced by both dichroism and anisotropic scattering. Mueller polarimetry is a powerful implementation of polarization sensing able to differentiate and measure the anisotropies of specimens. In this article, near infrared transmission Mueller scanning microscopy is used to image LD in thin biological specimen sections made of various proteins with unprecedented resolution and sensitivity. The near infrared spectral range makes it possible to lower the contribution of dichroism to the total linear diattenuation in order to highlight anisotropic scattering. Pixel-by-pixel comparison of LD images with LR and multiphoton images demonstrates that LD is produced by under-resolved structures that are not revealed by other means, notably within the sarcomere of skeletal muscles. LD microscopy appears as a powerful tool to provide new insights into the macro-molecular organization of biological specimens at the sub-microscopic scale without labelling.

1. Introduction

Light polarization is transformed after its interaction with complex biological specimens because of absorption, refraction and scattering processes that produce phase and/or amplitude anisotropies (birefringence and dichroism) [1]. At the microscopic scale, these anisotropies originate from the molecular order, and more specifically from the regular alignment of chemical bonds within organized structures. Biological structures such as lipid membranes, protein filament arrays (collagen fibrils and fibers, elastic fibers, filamentous myosin, microtubules, etc.) or nerve fibers are likely to produce linear anisotropies, whereas arrangements made of chiral biomolecules can induce circular anisotropies. Detection and mapping of these anisotropies have played an important role in biomedical imaging and diagnosis due to the high sensitivity of light polarization to the microstructural organization within tissues and cells [2,3].

Diattenuation quantifies the differential attenuation between two input orthogonal polarization states (linear or circular), and originates either from anisotropic absorption or anisotropic scattering [2]. Diattenuation caused by anisotropic absorption is often referred to linear dichroism (named LD_A) and circular dichroism (CD), respectively for linear and circular polarized light. LD_A has been used to establish the relative orientations of subunits in proteins and protein

orientation in membranes whereas CD provides powerful information on the short-range chiral order and composition of biomolecules [4–6]. As these effects are significant in the absorption bands of biomolecules, non-imaging LD_A and CD experiments have been mainly spectrally resolved in the UV/visible range. LD_A microscopy has however been demonstrated in the visible range but most of the experiments have been performed on stained specimens to enhance absorption [7–9]. Diattenuation can also result from anisotropic scattering (also called differential scattering) [10,11]. In the case of linearly polarized light, it will be named LD_S as follows. In the case of circularly polarized light, a technique referred as Circular Intensity Differential Scattering (CIDS) was developed to study the long-range chiral order and conformation of biomolecular arrangements [12–14]. Anisotropic absorption (LD_A and CD) and anisotropic scattering (LD_S and CIDS) are usually mixed within a specimen [15] but outside the absorption bands of the molecules, only anisotropic scattering is significant [16,17].

Only a few studies have so far been dedicated to linear diattenuation (LD) imaging of unstained biological tissues and cells [18–23]. Indeed, polarization microscopy of thin sections has mainly focused on linear retardance (LR) imaging, birefringence being the main source of contrast in tissues and cells [24–28]. Basic implementations of polarizing microscopy has enabled the generation of pure diattenuation images even in the presence of retardance, but failed to generate pure retardance images in the presence of diattenuation [22,23]. Mueller polarimetry is a powerful implementation of polarization sensing able to record and separate different types of anisotropies when they mix within a specimen [29]. Full-field Mueller imaging of bulk tissues was principally explored because it is able to also deal with the strong depolarization of light produced by multiple scattering. It has been successfully demonstrated in several biomedical and even preclinical studies [30,31]. Label-free Mueller microscopy is also an appropriate tool to perform retardance and diattenuation imaging of thin sections with good accuracy and sensitivity when the effects are mixed [32–35]. However, most experiments are conducted in the visible range, making diattenuation images difficult to interpret because of the contribution of both LD_A and LD_S, whose balance depends on experimental settings (wavelength, collection geometry) and on the sample itself. Indeed, absorption mainly results from molecular effects (composition, concentration) whereas scattering is rather a consequence of morphological effects (size, orientation and distribution of the scatterers). This might explain why diattenuation imaging has long been considered as being of secondary interest, although its potential has been recently demonstrated to provide powerful information on the microstructure of tissues composed of fibrous structures like nerve fibers in brain tissue sections [36].

Our group has recently developed a fast Mueller laser scanning microscope [37,38] based on a 1060 nm-swept laser source and spectral encoding of polarization [39]. The instrument is able to measure a full Mueller matrix in 10 µs from a set of around 1,000 intensity measurements [40], resulting in high sensitivity and a high acquisition rate. The near infrared wavelength range of the source makes it possible to work outside the absorption bands of most biomolecules and thus to lower the contribution of LD_A to the benefit of LD_S. In this study, we show the potential of label-free near infrared LD imaging of biological specimens at the microscopic scale. We have performed LD and LR laser scanning microscopy of two samples made of various proteins: a rabbit aortic wall transverse section and a rat skeletal muscle longitudinal section. By comparing pixel-by-pixel LD, LR and multiphoton images, we have observed that LD is produced by small and well-aligned macromolecular structures and can generate contrasts that are not revealed by the other imaging modalities, particularly within the sarcomere of skeletal muscles. Near infrared LD imaging thus appears to be a promising tool for providing new insights into the macro-molecular organization of biological specimens at the sub-microscopic scale without labelling.

2.   Materials and methods

2.1.   *Experimental setup*

The multimodal microscope used for the experiments is schematized in Fig. 1. It is composed of one Mueller matrix and two multiphoton imaging modalities (Polarization-resolved Second Harmonic Generation P-SHG and Two-Photon Excitation Fluorescence TPEF).
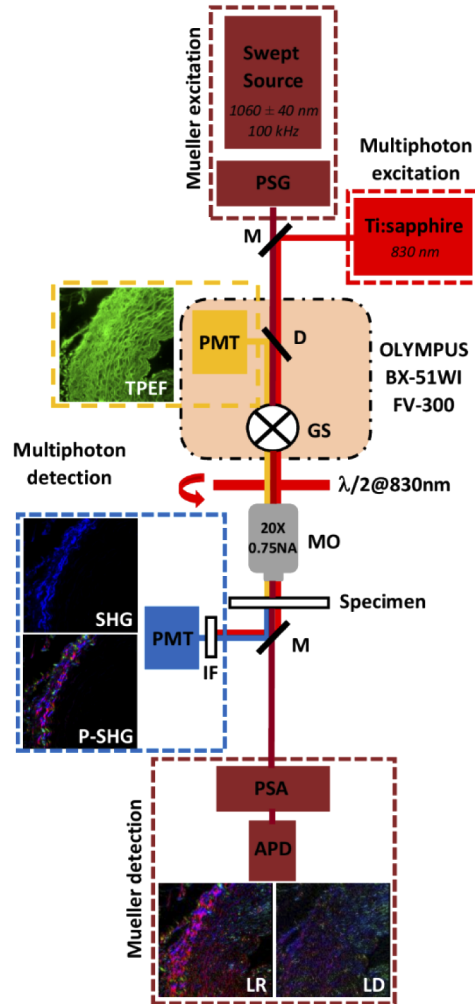

Fig. 1. Multimodal microscope composed of one Mueller matrix and two multiphoton imaging modalities. M: flip mirror. GS: galvo scanners. MO: microscope objective. Mueller matrix imaging modality: PSG (Polarization State Generator), PSA (Polarization State Analyzer), APD (Avalanche Photo Diode). Multiphoton imaging modality: PMT (Photo Multiplier Tube), IF (Interferential Filter), D (Dichroic mirror).

The microscope body is an upright confocal scanning microscope (BX51WI, Olympus) equipped with a galvo-galvo scanning head (FV300).

The Mueller imaging modality uses a swept laser source centered at 1060 nm (SSOCT-1060, Axsun Tech. Inc.) that sweeps the wavelength over a spectral range of 80 nm at a rate of 100 kHz. The polarization state generator (PSG) and analyzer (PSA) incorporate a linear polarizer oriented at 0° and 90°, high order YVO_4 retarders oriented at 0° and 45°, all the optical elements in the PSG

and PSA being fixed. The transmitted optical signal was detected by an avalanche photodiode (APD module C12703SPL, Hamamatsu) that delivers an analog voltage further digitized by a data acquisition board (DAQ, ATS9350 digitizer, AlazarTech). Although synchronization between the swept source, the galvo scanners and the DAQ is not represented in Fig. 1, the details can be found in Ref. [37]. The digitized signal consists of a succession of channeled spectra. Each channeled spectrum corresponds to each pixel location of the image and includes modulations that are specific to the polarimetric signature of the specimen. Signal processing (windowing, Fourier transform and matrix inversion) are performed to extract Mueller components for each pixel, and then polarimetric features (linear retardance/diattenuation magnitude and orientation) are calculated via a Lu and Chipman decomposition of the Mueller matrices [41].

The multiphoton imaging modality implements a Ti:sapphire femtosecond oscillator (Mira 900F-Verdi5, Coherent) tuned at 830 nm. The SHG signal is detected in transmission through a 415/10 nm interferential filter by a photomultiplier module (H10721-210, Hamamatsu). P-SHG images are obtained by acquiring 4 SHG images corresponding to 4 input linear polarizations, in order to extract the main orientation of collagen and myosin fibers [42]. A half-wave plate at 830 nm placed just before the microscope objective is used to rotate incident linear polarization. The backward TPEF signal is epi-detected through the internal descanned optical path of the confocal microscope, from which the pinhole is removed. A dichroic mirror is set to transmit the excitation laser beam and to back reflect the fluorescence from the sample.

Flip mirrors were added to switch between Mueller and multiphoton imaging modalities. A 20X/0.75NA microscope objective (UPlanSApo, Olympus) was used for all experiments, leading to theoretical diffraction-limited lateral resolution – defined as the full width at half maximum (FWHM) extent of the microscope point spread function (PSF) – of $\approx$ 560 nm for Mueller images [43] and $\approx$ 410 nm for multiphoton images [44]. Theoretical axial extents of the PSFs were $\approx$ 2.6 µm and $\approx$ 1.5 µm for Mueller matrix and multiphoton imaging, respectively. The 0.75NA objective is a good trade-off between high enough spatial resolution and moderate polarimetric distortions [45]. Images of 512×512 pixels were acquired for both modalities with a pixel-dwell time of 10 µs. The optical beams were superimposed to acquire images of the same regions of interest, thereby enabling pixel-by-pixel comparison between Mueller and multiphoton images.

2.2. Mueller matrix and multiphoton images

Mueller matrix images were acquired with a custom Labview software and processed under Matlab. For each pixel of the image, the Lu and Chipman decomposition was used to extract the polarimetric features. It consists in decomposing an experimental Mueller matrix into the product of three matrices representing pure polarimetric elements: a diattenuator, a depolarizer and a retarder. The retardance $\overrightarrow{R} = \begin{bmatrix} R_H & R_{45} & R_C \end{bmatrix}$ and diattenuation $\overrightarrow{D} = \begin{bmatrix} D_H & D_{45} & D_C \end{bmatrix}$ vectors are then derived in order to calculate the magnitudes of linear retardance (LR) and linear diattenuation (LD), and their orientations φ_R and φ_D:

$$LR = \sqrt{R_H^2 + R_{45}^2}, \quad \varphi_R = \arctan\left(\frac{R_{45}}{R_H}\right) \tag{1}$$

$$LD = \sqrt{D_H^2 + D_{45}^2}, \quad \varphi_D = \arctan\left(\frac{D_{45}}{D_H}\right) \tag{2}$$

The parameters extracted from the Lu and Chipman decomposition are linked to the following definitions of retardance and diattenuation:

$$R = |\delta_q - \delta_r| \tag{3}$$

$$D = \frac{T_q - T_r}{T_q + T_r} \tag{4}$$

where R = $|\vec{R}|$, D = $|\vec{D}|$, δ_q and δ_r are the phase changes for each eigen-polarization, T_q and T_r are the transmittance for each eigen-polarization. The Lu and Chipman decomposition is well suited for thin specimen sections where light depolarization is weak. Images are displayed using a Hue Saturation Value (HSV) colormap where Hue represents the orientation φ_R or φ_D and V represents the magnitude of LR or LD. The 0° angle aligns with the horizontal side of the images. LR and LD images encoded in magnitude only were presented in the supplemental document (Fig. S2 for the aorta and Fig. S3 for the muscle).

Multiphoton images were acquired using the software of the scanning microscope (FluoView), providing 12-bit grayscale images in TIFF format. TPEF and SHG images are displayed using a RGB colormap, in which TPEF is encoded in the green channel and SHG in the blue channel. For merged TPEF/SHG images, both channels are used simultaneously, leading to cyan areas when TPEF and SHG signals overlap. P-SHG images are built with a HSV colormap where Hue represents the in-plane orientation of the fibers and V the magnitude of SHG.

2.3. Biological specimen sections

The rabbit aortic wall cross section was taken from a set of specimens from a previous study [46] that was performed in accordance with the European Council revised guidelines on animal care for experimental and other scientific purposes, and approved by the local ethic committee for animal experimentation (authorization number: CEEA.2012.189). The study was performed on 3 month-old male homozygous Watanabe heritable hyperlipidemic (WHHL) rabbits produced by CPA Jeanrot (FRANCE, 45160 Olivet). Aorta samples were extracted and fixed in Bouin's solution for 48 hours and then embedded in paraffin. Transverse section of 5 μm thickness were cut by a microtom, then deparaffined and mounted with Neo-Mount® (Merck Millipore 109016) between a microscope slide and a 170 μm-thick coverslip.

The rat striated muscle longitudinal section was also taken from a set of specimens of a previous study [47], for which 3 months-old female Wistar rats were sacrificed in accordance with the local committee of ethic protocol (authorization 02076.01). Extensor Digitorum Longus (EDL) muscles were removed from the hind limb, fixed in 4% paraformaldehyde at the resting length and embedded in Optimal Cutting Temperature (OCT) compound. Histological slices of 10 μm thickness were produced by a cryotom in the longitudinal direction of the myofibrils.

Both samples have experienced a classical preparation process for microscopy observation, enabling to compare the results with other studies. Although some optical parameters (scattering and absorption coefficients) can be slightly affected by the sample preparation [48], it was assumed that polarimetric parameters were not much affected because they are mostly depending on the tissue structure rather than on the molecular environment.

The axial extent of the PSF of the Mueller modality being a few times smaller than the thickness of the sections and because Mueller imaging has no inherent axial sectioning, it was ensured that no structures were overlapping in the axial direction by performing z-stack multiphoton imaging prior to Mueller imaging, and selecting regions of interest exhibiting good homogeneity in the axial direction. Muscle transverse sections of 6 μm-thickness were experienced and gave the same behavior for the polarimetric parameters, with however a slight lower signal-to-noise ratio for the Mueller images because of the lower optical path encountered by light.

3. Results

3.1. Imaging of rabbit aortic wall cross section

Multiphoton and Mueller matrix images of a rabbit aortic wall cross section are displayed in Fig. 2, as well as line profiles across the section of the aorta.

Aortic wall is mainly composed of three layers: a thin inner layer rich in endothelial cells, a thick middle layer principally made of smooth muscle and elastic fibers that confer its elasticity to
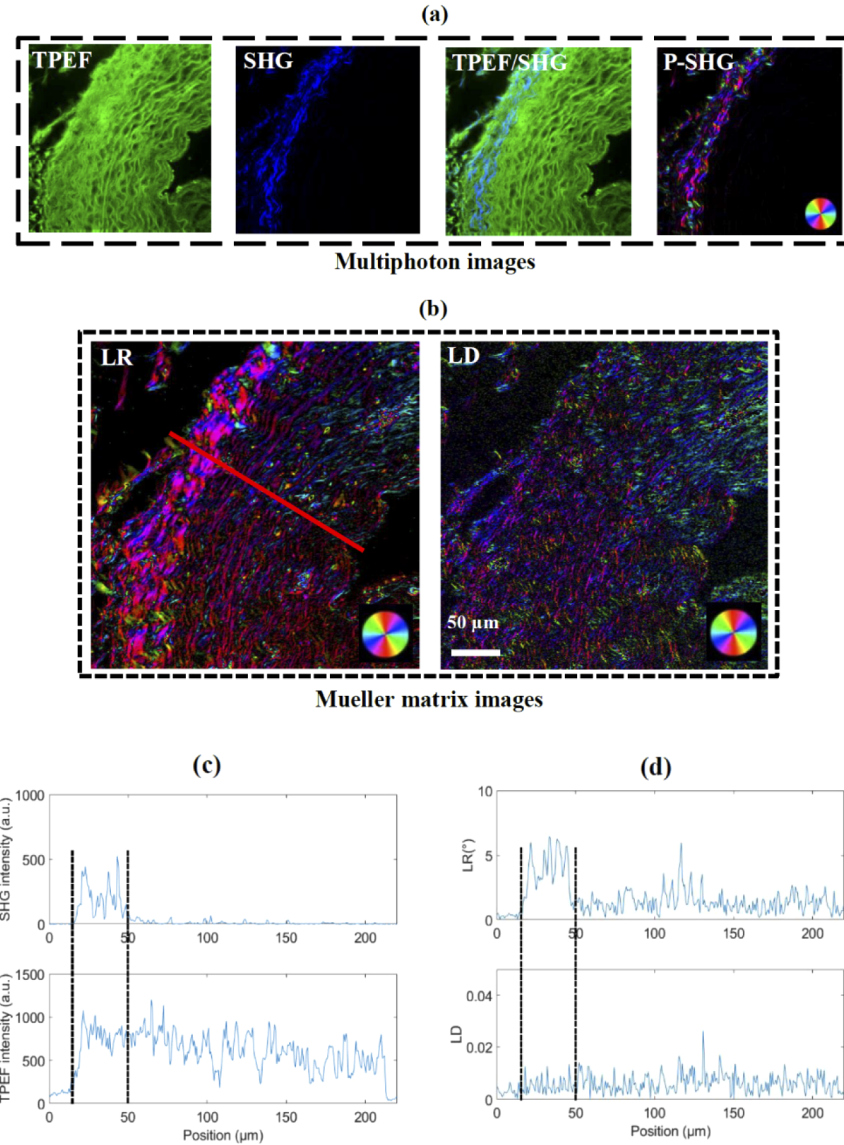
Fig. 2. Multimodal imaging of a rabbit aortic wall cross section (thickness 5 µm). (a) Multiphoton images including TPEF, SHG, merged TPEF/SHG and P-SHG. The P-SHG image displays the orientation of collagen fibers. (b) Mueller images (5 times averaging), including LR and LD images, encoded in the HSV colormap described in Methods. The V channel range corresponds to a magnitude of LR and LD respectively between 0° and 10°, and 0 and 0.03. (c) SHG and TPEF intensity profiles along the red line displayed in the LR image. (d) LR and LD magnitudes profiles along the red line displayed in the LR image. The dotted black lines delimit the outer region of the aorta that contains type I-collagen.

the aorta, and a thinner outer rigid layer composed of collagen fibers. The TPEF image exhibits quite a significant background, associated with the residual fluorescence emission by cellular NAD(P)H and fibroblasts at this excitation wavelength (830 nm), but that also reveals a strong fibrous lamellar structure located in the middle region of the aortic wall that is attributed to the fluorescence emission by elastin [49]. SHG is mainly located in the outer layer of the aortic wall, which reveals a strong density of type I-collagen fibers, as expected. In the regions of strong SHG signals, TPEF tends to be lower indicating a lower density of elastic fibers in the outer layer. P-SHG image represents the main orientation of the SHG emitters within collagen fibers, and reveals the orientation of the fibers themselves, as already demonstrated [50].

Among the set of polarimetric parameters available from the Mueller matrices, only LR and LD showed significant contrast and are thus displayed. LR is significantly stronger in the outer region of the aortic wall and exhibits a more dispersed fibrous lamellar structure in the middle region. Magnitude of LR extend from 0° to 2-3° inside the middle region and can reach approximatively 8° inside the outer layer. Comparison between LR and multiphoton images confirms that retardance is produced by both elastin and collagen fibers [1]. Indeed, areas of high LR overlap with areas of high SHG (see profiles of Figs. 2(c) and 2(d)), which are characteristic of regions rich in type I-collagen. LR is also significant in the middle region of the aorta and exhibits a lamellar fibrous aspect close to the one observed in the TPEF image. This indicates that elastin fibers also contribute to retardance, with relatively lower magnitude in comparison to collagen. Because retardance is a cumulative effect, it is higher when the fibers are densely packed and lower for isolated and smaller fibers. It should be noticed that the orientation of LR is the same as the in-plane orientation of the fibers given by P-SHG (see Fig. S1 for higher definition images), this direction being expected to be parallel to the average direction of the conjugate bonds within the collagen triple helix that is along the axis of the fibers. Correlation between SHG and LR from collagen fibers has already been established [51–53]. However, these previous studies were based on two distinct microscopes for Mueller and multiphoton imaging, the resolution of the former being much worse than that of the latter. In addition, SHG imaging was not resolved in polarization. In our study, the orientation fields of collagen fibers are compared pixel-by-pixel from Mueller and P-SHG images obtained from the same scanning microscope at nearly the same spatial resolution.

The LD image is characteristically different, and is rather homogeneous with values of diattenuation ranging from 0.01 to 0.02. Particularly, LD does not exhibit stronger magnitudes in the outer region (see profile of Fig. 2(d)), indicating that diattenuation mainly originates from LD_S, as expected in the near infrared range. Indeed, LD_A would have produced stronger diattenuation values in the outer region composed of a higher density of fibers, as in the retardance image. Moreover, it can be noticed that only small fibers or fibrils with approximatively the same size are revealed in the LD image. The diameter of these small fibers or fibrils is close to the diffraction limit of the Mueller imaging modality, indicating that LD is mainly produced by small fibers or fibrils whose diameter is under or near the resolution limit of the microscope. This behavior is also consistent with LD_S that tends to be higher when the diameter of the fibers decreases [36]. It can also be noticed that several small fibers or fibrils are evidenced in the LD image but not in the LR image (Fig. S2), demonstrating that LD and LR does not necessarily reveal the same structures within the specimen. Finally, we observe that the orientation of LD is parallel to the fibers. This direction is the same as the orientation of LR, which is consistent with the results obtained in [36] on nerve fibers.

3.2. Imaging of rat striated muscle longitudinal section

Multiphoton and Mueller matrix images of a rat striated skeletal muscle longitudinal section are presented in Fig. 3, as well as their profile along the main direction of the myofibril.
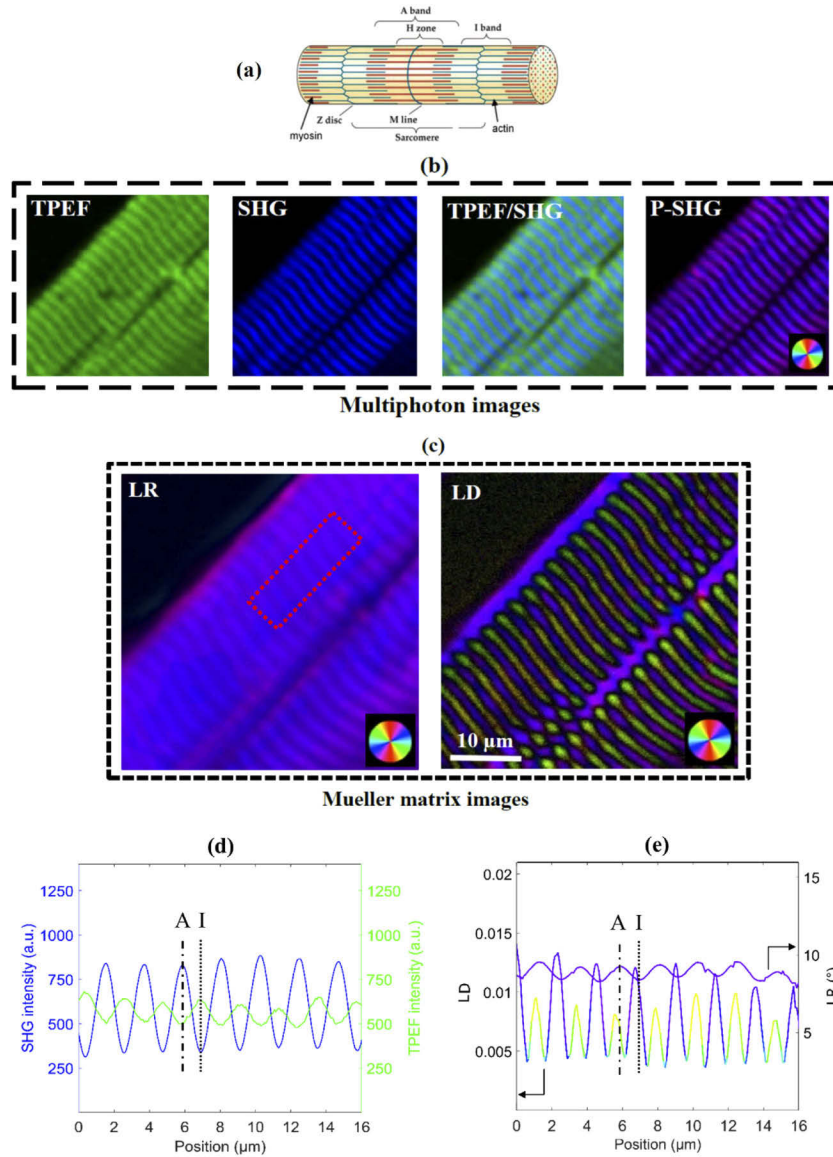
Fig. 3. Multimodal imaging of a rat striated muscle fiber longitudinal section (thickness 10 μm). (a) Schematic representation of the sarcomere of a myofibril. (b) Multiphoton images including TPEF, SHG, merged TPEF/SHG and P-SHG. The P-SHG image displays the orientation of myosin filaments. (c) Mueller matrix images (5 times averaging), including LR and LD images, encoded in the HSV colormap described in Methods. The V channel range corresponds to a magnitude of LR (respectively LD) between 0° and 15° (respectively between 0 and 0.03). (d) SHG and TPEF intensity profiles (e) LD and LR magnitude profiles. The color of the line represents the orientation of LD/LR, according to the same colormap as the one used for the images. The profiles were obtained by first binning the values within the red dotted rectangle along the transverse direction of the myofibril, and then plotting these values versus the longitudinal direction. Two vertical dashed lines were superimposed to the profiles in order to locate the center of the A band and the I band.

In striated skeletal muscle of mammals, myofibrils have a cylinder shape and are composed of a complex but regular organization of proteins (Fig. 3(a)). The isotropic I band, that appears bright in bright-field and transmission electron microscopy, is mainly composed of thin actin filaments, whereas the anisotropic A band, that appears dark in transmission electron microscopy but bright in cross-polarized optical microscopy, is mainly composed of thick myosin filaments with a region of overlapping with thin actin filaments. The M-line is located in the center of the A band and the Z-disc is located in the center of the I band. The basic unit between two Z-discs is called the sarcomere, whose length is typically between 2-3 μm in mammals at rest.

TPEF and SHG images exhibit complementary contrasts, evidenced by the merged TPEF/SHG image (Fig. 3(b)) and the longitudinal intensity profile (Fig. 3(d)), as already established [42]. Indeed, for symmetry reasons, SHG is exclusively produced by myosin thick filaments, enabling locating the A band within the sarcomere [54]. Fluorescence emission is stronger in the I band, indicating that actin thin filaments have a stronger fluorescent emission that myosin thick filaments. P-SHG image confirms that the mean orientation of myosin filaments is parallel to the myofibril direction [42], depicted here at about +45° from the horizontal side of the image.

The LR image has a similar pattern as the SHG profile, indicating that LR is stronger in the A band mostly composed of thick myosin filaments. The values of LR oscillates between 8° and 10°, which is consistent with previous reported values [55,56]. The contrast of the LR image is less than that of the SHG image, which could be first explained because birefringence is a cumulative effect resulting from light propagation through the whole sample thickness. Indeed, unlike multiphoton microscopy, Mueller matrix microscopy has no inherent axial sectioning because it deals with linear light-matter interaction processes. LR is thus likely to be produced by sarcomeres above and below the Rayleigh range of the microscope objective lens (≈ 2.6 μm) which is significantly lower than the thickness of the section (≈ 10 μm) in our experiments. If the sarcomeres do not overlap perfectly in the axial direction this could result in a residual retardance in the I bands. Secondly, the width of each band is close to the spatial resolution of the Mueller matrix imaging modality which could explain the lower contrast of the retardance image. Finally, thin actin filaments can produce small but detectable LR. The orientation of LR is along the direction of the myofibril and in accordance with the orientation of the fibers given by the P-SHG image, i.e., at about +45° from the horizontal side of the image.

The most striking result comes from the behavior of diattenuation. Indeed, the LD image exhibits a regular and well-resolved double band pattern with alternating orientations (Fig. 3(c)) that is not evidenced in the LR and multiphoton images. Moreover, maxima of LD magnitude do not perfectly superimpose with extrema of LR, indicating that LD is not produced by the same structures that produce birefringence. LD is significant in the areas of lower retardance (I bands), but also in the areas of higher retardance (A bands), as evidenced in Fig. 3(e). LD appears higher near the center of I bands than near the center of A bands. The resolution of the Mueller matrix imaging modality being very close to the size of a single band (A or I), it is interesting to notice the thin regions of minimum diattenuation between two maxima. The size of these "dark" regions seems to be slightly under the resolution limit of the Mueller modality, showing the possibility to image under-resolved structures with LD imaging. It has been demonstrated in the previous section of the paper that only small fibers are likely to generate LD, regions of densely packed fibers being more suited to produce stronger LR. At the sarcomere scale, LD is thus not expected to emerge from regions with a high density of myosin and actin filaments, but is probably due to smaller but well-aligned structures within the M-band and the Z-disc. The orientation profiles in Fig. 3(e) indicate that the orientation of LR is always parallel to the myofibril, but the orientation of LD is perpendicular to the myofibril in the A band and parallel to the myofibril in the I band. Given that LD orientation is parallel to the principal axis of the structure producing anisotropic scattering, we suggest that LD is produced by structures along the direction of the M-line in the A band and in a direction perpendicular to the Z-disc in the I band. It should be emphasize

that the crossed orientations of LD between the two bands is able to explain the appearance of a thin region of very low diattenuation between the two bands. Particularly, considering that summation of optical waves scattered by two orthogonal infinitely long cylinders of diameter below the wavelength may produce sub-resolution regions of lower diattenuation [10,11].

4. Discussion

For elastic light-matter interaction processes, the same anisotropy which leads to retardance can also yield to diattenuation. Indeed, retardance and LD_A are closely related because they are associated respectively to the real and imaginary part of the refractive index. In biological specimens, most of the molecules absorb in the ultraviolet but residual anisotropy can still be observable in the visible range, depending on the strength and the width of the resonance [22]. Absorption can also be enhanced in the visible part of the spectrum by staining the samples with specific dyes like Picrosirius red for collagen for instance [9]. As a consequence, LD_A and LR images usually carry strongly correlated information on the structure under investigation. Because linear dichroism is a molecular effect, it depends on molecular composition and concentration. For filamentous/fibrous structures, birefringence has mainly been used to display in-plane and out-of-plane filaments/fibers in polarizing microscopy [24–26] but very little attention has been devoted to linear diattenuation imaging. Diattenuation by anisotropic scattering, or LD_S, can also be produced by long-shape biomolecular arrays like filamentous arrays or organized structures. Indeed, analytical modelling of a single scattering event by an infinite cylinder in the Rayleigh-Gans regime reveals that light polarized parallel to the cylinder is differently attenuated that light polarized perpendicular to the cylinder [10,11]. The magnitude of diattenuation caused by anisotropic scattering depends, at the microscopic scale, on many parameters like the cylinder diameter, its relative refractive index in comparison to the one of the surrounding medium, and the density and organization of the cylinders.

In a recent study by Menzel *et al.* [36], numerical computation of Maxwell's equations and analytical modelling was used to explain the origin of linear diattenuation observed in brain tissue sections. The study considered diattenuation by anisotropic scattering (LD_S), as well as diattenuation by anisotropic absorption (LD_A). Indeed, because the experiments were driven in the visible range, both effects had to be taken into account. It was demonstrated that LD_S was mainly produced by small nerve fibers lying in the plane of the sections, whereas LD_A was generated by the myelin sheath, particularly by the myelin lipids that are oriented perpendicularly to the nerve fibers. The diameters of the nerve fibers ranged from 0.3 μm to 1 μm and the orientation of LD was found to be parallel to the nerve fibers. The magnitude of experimental linear diattenuation ranged from 0 to 0.02, which is close to the values obtained in our study. Another very recent study by Li *et al.* [57], including polarization-resolved Monte Carlo simulations and Mueller matrix experiments on skin dermis biomimetic phantoms, also highlighted the possibility to detect LD_S in thin sections in a transmission microscopy geometry. The scattering coefficient of the tissue was set to 500 cm^{-1}, no absorption was considered and scattering cylinders of radius 0.05 μm mimicking small collagen fibrils were included in the model. It resulted in values of linear diattenuation between 0 and 0.05 for 5 μm thickness sections, which is also in close accordance with the values obtained in our experiments. Finally, Das *et al.* [58] have noticed an interesting behavior of spectral linear diattenuation in backscattering non-imaging experiments on random scattering media made of small scatterers, with a potential for screening subtle micro-structural changes associated with cancer progression. All of these recent studies [36,57,58], based on numerical simulations and experiments, demonstrated that LDs can be observed in thin sections of unstained biological material, as a consequence of anisotropic scattering by filaments or structures of diameters below or of the order of the diffraction limit.

In our study this is the first time, to the best of our knowledge, that near infrared LD images of biological specimens are presented at such high resolution and sensitivity. The near infrared

spectral range (1060 nm) of the source enables us to lower dichroism and highlight anisotropic scattering in the overall measured linear diattenuation. Light is indeed preferably scattered than absorbed by biological tissues in the near infrared. Indeed, absorption and scattering coefficients are of the order of 1 cm^{-1} and 100 cm^{-1}, respectively [59,60]. Although these values are macroscopic and results from light propagation within large volumes of tissue, some works were dedicated to the measurement of the optical parameters of the principal proteins that compose aorta (elastin, collagen) [61], or were spatially-resolved in the case of muscle [62]. In these studies, the absorption coefficients were still under 1 cm^{-1}. However, absorption coefficients only sign isotropic absorption by a specimen, but a simple analytical model can be used to evaluate the maximum value of diattenuation caused by anisotropic absorption that can be obtained with a given isotropic absorption. The diattenuation in Eq. (4) can be reformulated as follows:

$$D = \frac{T_q - T_r}{2T_u} \tag{5}$$

where $T_u = 1/2(T_q + T_r)$ is the unpolarized transmittance that is linked to isotropic absorption. If T_u is close to 1 (low isotropic absorption), the maximum value for T_q is 1 and thus $T_r = (2T_u - 1)$, leading to:

$$D^{max} = \frac{1 - T_u}{T_u} \approx 1 - T_u \tag{6}$$

Considering specimens of 5 and 10 μm-thickness, a 1 cm^{-1} absorption coefficient provides an unpolarized transmittance of 0.9995 and 0.999, respectively, which means maximum values of diattenuation of 0.0005 and 0.001. These values of diattenuation are below the minimum detectable values with our setup. LD$_A$ was thus not expected to be significant in these experiments, all the more no dye was added to the specimens. This was also confirmed because no correlation was observed between the magnitudes of retardance and diattenuation in aorta and muscle (profiles of Figs. 2 and 3). The moderate numerical aperture of the microscope objective used in this study enabled the imaging of LD with good lateral resolution, while limiting polarization distortions. We observed that LD is mainly produced by very small filamentous arrays or well-aligned structures, whose diameter is probably well below the spatial resolution of our scanning microscope. Particularly, the resolution of the LD images enabled us to visualize the structural organization within the sarcomere of a myofibril. The high selectivity and sensitivity of the Mueller matrix microscope was necessary to deal with weak values of diattenuation and retardance with a high enough signal-to-noise ratio. Indeed, it should be emphasized that a diattenuation of 0.01 provides an intensity change of about 0.01% in classical polarized light microscopy whereas a retardance of 8° leads to a change of about 8% of the intensity. Therefore, diattenuation is hardly detectable while being easily masked by retardance in a standard polarization microscope. This makes Mueller matrix scanning microscopy a powerful tool for the detection and imaging of weak, mixed anisotropies.

Anisotropic scattering by muscle fibers was already explored using Mueller matrix polarimetry [63], but the cylinders were associated with large myofibrils of 1-2μm diameter because the lack of spatial resolution did not allow visualization of the inner microstructure of the myofibrils. In our study, we demonstrated that LD is in fact related to the structural organization within the myofibril. LD and LR magnitude and orientation profiles indicated that LD and LR are not produced by the same structures. Although the orientation of LD gives insight into the possible microstructures responsible for this effect, it is premature at this stage to conclude on the origin of the double band revealed by LD, because it lacks specificity to the molecular composition. However, LD appears as a powerful tool for probing muscular microscopic organization and changes at the sarcomere scale.

5. Conclusion

In this article, we have presented near infrared linear diattenuation (LD) and linear retardance (LR) images of aortic wall and skeletal muscle sections with unprecedented spatial resolution and sensitivity. We have observed that LD is produced by small filamentous macromolecular arrays whose diameter is below the expected spatial resolution of the microscope. LD has been able to generate within the sarcomere of a skeletal muscle, a surprising double band pattern with alternating perpendicular orientations that was not revealed by other imaging modalities like LR, TPEF and SHG microscopies. Although lacking specificity, LD imaging appears to be a promising tool to give new insights into the macro-molecular organization of biological specimens at the sub-microscopic scale without labelling. Performing multispectral LD imaging in both the visible and near infrared spectral range will enable us to gain more insight into the origin and behavior of linear diattenuation in thin tissue sections. This should be made possible soon, by implementing recent developments in dual wavelength swept laser sources [64].

Acknowledgments

Disclosures

The authors declare that there are no conflicts of interest related to this article.

See Supplement 1 for supporting content.

References

1. V. V. Tuchin, "Polarized light interaction with tissues," J. Biomed. Opt. **21**(7), 071114 (2016).
2. N. Gosh and I. A. Vitkin, "Tissue polarimetry: concepts, challenges, applications, and outlook," J. Biomed. Opt. **16**(11), 110801 (2011).
3. V.V. Tuchin, L.V. Wang, and D.A. Zimnyakov, "Optical Polarization in Biomedical Applications", New York, USA (2006).
4. B. Ranjbar and P. Gill, "Circular dichroism techniques: biomolecular and nanostructural analyses- a review," Chem. Biol. Drug Des. **74**(2), 101–120 (2009).
5. B. M. Bulheller, A. Rodger, and J. D. Hirst, "Circular and linear dichroism of proteins," Phys. Chem. Chem. Phys. **9**(17), 2020–2035 (2007).
6. A. Rodger, G. Dorrington, and D. L. Ang, "Linear dichroism as a probe of molecular structure and interactions," Analyst **141**(24), 6490–6498 (2016).
7. B. de Campos Vidal, E. H. Dos Anjos, and M. L. Mello, "Optical anisotropy reveals molecular order in a mouse enthesis," Cell Tissue Res. **362**(1), 177–185 (2015).
8. L.-W. Jin, K. A. Claborn, M. Kurimoto, M. A. Geday, I. Maezawa, F. Sohraby, M. Estrada, W. Kaminksy, and B. Kahr, "Imaging linear birefringence and dichroism in cerebral amyloid pathologies," Proc. Natl. Acad. Sci. U. S. A. **100**(26), 15294–15298 (2003).
9. B. Laude-Boulesteix, A. De Martino, B. Drévillon, and L. Schwartz, "Mueller polarimetric imaging system with liquid crystals," Appl. Opt. **43**(14), 2824–2832 (2004).
10. C.F. Bohren and D.R. Huffman, "*Absorption and Scattering of Light by Small Particles*", (John Wiley and Sons, 1983).
11. H.C. Van de Hulst, "*Light scattering by small particles*", (John Wiley and Sons, 1957).
12. C. Bustamante, M. F. Maestre, and I. Tinoco Jr., "Circular intensity differential scattering of light by helical structures. I. Theory," J. Chem. Phys. **73**(9), 4273–4281 (1980).
13. A. Sharma, A. Campbell, J. Leoni, Y. T. Cheng, M. Müllner, and G. Lakhwan, "Circular Intensity Differential Scattering Reveals the Internal Structure of Polymer Fibrils," J. Phys. Chem. Lett. **10**(24), 7547–7553 (2019).
14. A. Diaspro and C. A. Nicolini, "Circular intensity differential scattering and chromatin-DNA structure," Cell Biophys. **10**(1), 45–60 (1987).

15. C. Bustamante, I. Tinoco Jr., and M. F. Maestre, "Circular differential scattering can be an important part of the circular dichroism of macromolecules," Proc. Natl. Acad. Sci. U. S. A. **80**(12), 3568–3572 (1983).
16. A. Le Gratiet, L. Pesce, M. Oneto, R. Marongiu, G. Zanini, P. Bianchini, and A. Diaspro, "Circular intensity differential scattering (CIDS) scanning microscopy to image chromatin-DNA nuclear organization," OSA Continuum **1**(3), 1068–1078 (2018).
17. R. Marongiu, A. Le Gratiet, L. Pesce, P. Bianchini, and A. Diaspro, "ExCIDS: a combined approach coupling Expansion Microscopy (ExM) and Circular Intensity Differential Scattering (CIDS) for chromatin-DNA imaging," OSA Continuum **3**(7), 1770–1780 (2020).
18. A. Vitkin, N. Ghosh, and A. D. Martino in: *Tissue Polarimetry* (John Wiley & Sons, Inc., 2015), pp. 239–321.
19. P. Rzeczycki, G. S. Yoon, R. K. Keswani, S. Sud, K. A. Stringer, and G. R. Rosania, "Detecting ordered small molecule drug aggregates in live macrophages: a multi-parameter microscope image data acquisition and analysis strategy," Biomed. Opt. Express **8**(2), 860–872 (2017).
20. K. A. Min, W. G. Rajeswaran, R. Oldenbourg, G. Harris, R. K. Keswani, M. Chiang, P. Rzeczycki, A. Talattof, M. Hafeez, R. W. Horobin, S. D. Larsen, K. A. Stringer, and G. R. Rosania, "Massive Bioaccumulation and Self-Assembly of Phenazine Compounds in Live Cells," Adv. Sci. **2**(8), 1500025 (2015).
21. O. K. Naoun, V. L. Dorr, P. Allé, J. C. Sablon, and A. M. Benoit, "Exploration of the retinal nerve fiber layer thickness by measurement of the linear dichroism," Appl. Opt. **44**(33), 7074–7082 (2005).
22. S. B. Mehta, M. Shribak, and R. Oldenburg, "Polarized light imaging of birefringence and diattenuation at high resolution and high sensitivity," J. Opt. **15**(9), 094007 (2013).
23. M. Menzel, J. Reckfort, D. Weigand, H. Köse, K. Amunts, and M. Axer, "Diattenuation of brain tissue and its impact on 3D polarized light imaging," Biomed. Opt. Express **8**(7), 3163–3197 (2017).
24. R. Oldenbourg, "A new view on polarization microscopy," Nature **381**(6585), 811–812 (1996).
25. M. F. G. Wood, N. Ghosh, M. A. Wallenburg, S.-H. Li, R. D. Weisel, B. C. Wilson, R.-K. Li, and I. A. Vitkin, "Polarization birefringence measurements for characterizing the myocardium, including healthy, infarcted, and stem-cell-regenerated tissues," J. Biomed. Opt. **15**(4), 047009 (2010).
26. M. Shribak and R. Oldenburg, "Techniques for fast and sensitive measurements of two-dimensional birefringence distributions," Appl. Opt. **42**(16), 3009–3017 (2003).
27. M. Axer, K. Amunts, D. Grässel, C. Palm, J. Dammers, H. Axer, U. Pietrzyk, and K. Zilles, "A novel approach to the human connectome: Ultra-high resolution mapping of fiber tracts in the brain," NeuroImage **54**(2), 1091–1101 (2011).
28. N.-J. Jan, K. Lathrop, and I. A. Sigal, "Collagen Architecture of the Posterior Pole: High-Resolution Wide Field of View Visualization and Analysis Using Polarized Light Microscopy," Invest. Ophthalmol. Visual Sci. **58**(2), 735–744 (2017).
29. R.A. Chipman, "Polarimetry," *Handbook of Optics* 2, 1–22, (McGraw-Hill, 1995).
30. S. Alali and A. Vitkin, "Polarized light imaging in biomedicine: emerging Mueller matrix methodologies for bulk tissue assessment," J. Biomed. Opt. **20**(6), 061104 (2015).
31. J. Qi and D. S. Elson, "Mueller polarimetric imaging for surgical and diagnostic applications: a review," J. Biophotonics **10**(8), 950–982 (2017).
32. H. He, R. Liao, N. Zeng, P. Li, Z. Chen, X. Liu, and H. Ma, "Mueller Matrix Polarimetry—An Emerging New Tool for Characterizing the Microstructural Feature of Complex Biological Specimen," J. Lightwave Technol. **37**(11), 2534–2548 (2019).
33. J. Qi, C. He, and D. S. Elson, "Real time complete Stokes polarimetric imager based on a linear polarizer array camera for tissue polarimetric imaging," Biomed. Opt. Express **8**(11), 4933–4946 (2017).
34. A. Le Gratiet, M. d'Amora, M. Duocastella, R. Marongiu, A. Bendandi, S. Giordani, P. Bianchini, and A. Diaspro, "Zebrafish structural development in Mueller-matrix scanning microscopy," Sci. Rep. **9**(1), 19974 (2019).
35. O. Arteaga, M. Baldrís, J. Antó, A. Canillas, E. Pascual, and E. Bertran, "Mueller matrix microscope with a dual continuous rotating compensator setup and digital demodulation," Appl. Opt. **53**(10), 2236–2245 (2014).
36. M. Menzel, M. Axer, K. Amunts, H. De Raedt, and K. Michielsen, "Diattenuation Imaging reveals different brain tissue properties," Sci. Rep. **9**(1), 1939 (2019).
37. A. Le Gratiet, M. Dubreuil, S. Rivet, and Y. Le Grand, "Scanning Mueller polarimetric microscopy," Opt. Lett. **41**(18), 4336–4339 (2016).
38. S. Rivet, M. Dubreuil, A. Bradu, and Y. Le Grand, "Fast spectrally encoded Mueller optical scanning microscopy," Sci. Rep. **9**(1), 3972 (2019).
39. M. Dubreuil, S. Rivet, B. Le Jeune, and J. Cariou, "Snapshot Mueller matrix polarimeter by wavelength polarization coding," Opt. Express **15**(21), 13660–13668 (2007).
40. A. Le Gratiet, S. Rivet, M. Dubreuil, and Y. Le Grand, "100kHz-Mueller polarimeter in reflection configuration," Opt. Lett. **40**(4), 645–648 (2015).
41. S. Y. Lu and R. A. Chipman, "Interpretation of Mueller matrices based on polar decomposition," J. Opt. Soc. Am. A **13**(5), 1106–1113 (1996).
42. C. Odin, T. Guilbert, A. Alkilani, O. P. Boryskina, V. Fleury, and Y. Le Grand, "Collagen and myosin characterization by orientation field second harmonic microscopy," Opt. Express **16**(20), 16151–16165 (2008).
43. A. Diaspro, "*Confocal and Two-Photon Microscopy: Foundations, Applications, and Advances*," (John Wiley and Sons, 2002).

44. W. R. Zipfel, R. M. Williams, and W. W. Webb, "Nonlinear magic: multiphoton microscopy in the biosciences," Nat. Biotechnol. **21**(11), 1369–1377 (2003).

45. B. Richards and E. Wolf, "Electromagnetic diffraction in optical systems. II. Structure of the image field in an aplanatic system," Proc. R. Soc. Lond. A **253**(1274), 358–379 (1959).

46. F. Tissier, Y. Mallem, C. Goanvec, R. Didier, T. Aubry, N. Bourgeois, J.-C. Desfontis, M. Dubreuil, Y. Le Grand, J. Mansourati, K. Pichavant-Rafini, E. Plee-Gautier, P. Roquefort, M. Theron, and M. Gilard, "A non-hypocholesterolemic atorvastatin treatment improves vessel elasticity by acting on elastin composition in WHHL rabbits," Atherosclerosis **251**, 70–77 (2016).

47. M. Dubreuil, F. Tissier, L. Le Roy, J.-P. Pennec, S. Rivet, M.-A. Giroux-Metges, and Y. Le Grand, "Polarization-resolved second harmonic microscopy of skeletal muscle in sepsis," Biomed. Opt. Express **9**(12), 6350–6358 (2018).

48. M. Mesradi, A. Genoux, V. Cuplov, D. Abi-Haidar, S. Jan, I. Buvat, and F. Pain, "Experimental and analytical comparative study of optical coefficient of fresh and frozen rat tissues," J. Biomed. Opt. **18**(11), 117010 (2013).

49. T. Boulesteix, A.-M. Pena, N. Pagès, G. Godeau, M.-P. Sauviat, E. Beaurepaire, and M.-C. Schanne-Klein, "Micrometer scale ex vivo multiphoton imaging of unstained arterial wall structure," Cytometry, Part A **69A**(1), 20–26 (2006).

50. C. Odin, Y. Le Grand, A. Renault, L. Gailhouste, and G. Baffet, "Orientation fields of nonlinear biological fibrils by second harmonic generation microscopy," J. Microsc. **229**(1), 32–38 (2008).

51. P. G. Ellingsen, M. B. Lilledahl, L. M. S. Aas, C. de Lange Davies, and M. Kildemo, "Quantitative characterization of articular cartilage using Mueller matrix imaging and multiphoton microscopy," J. Biomed. Opt. **16**(11), 116002 (2011).

52. P. G. Ellingsen, L. M. S. Aas, V. S. Hagen, R. Kumar, M. B. Lilledahl, and M. Kildemo, "Mueller matrix three-dimensional directional imaging of collagen fibers," J. Biomed. Opt. **19**(2), 026002 (2014).

53. S. Bancelin, A. Nazac, B. H. Ibrahim, P. Dokládal, E. Decencière, B. Teig, H. Haddad, H. Fernandez, M.-C. Schanne-Klein, and A. De Martino, "Determination of collagen fiber orientation in histological slides using Mueller microscopy and validation by second harmonic generation imaging," Opt. Express **22**(19), 22561–22574 (2014).

54. F. S. Pavone and P. J. Campagnola, "Second Harmonic Generation Imaging," in *Series in Cellular and Clinical Imaging,* (CRC Press, 2014).

55. R. C. Haskell, F. D. Carlson, and P. S. Blank, "Form birefringence of muscle," Biophys. J. **56**(2), 401–413 (1989).

56. M. Irving, "Birefringence changes associated with isometric contraction and rapid shortening steps in frog skeletal muscle fibers," J. Physiol. **472**(1), 127–156 (1993).

57. P. Li, H. R. Lee, S. Chandel, C. Lotz, F. K. Groeber-Becker, S. Dembski, R. Ossikovski, H. Ma, and T. Novikova, "Analysis of tissue microstructure with Mueller microscopy: logarithmic decomposition and Monte Carlo modeling," J. Biomed. Opt. **25**(1), 1 (2020).

58. N. K. Das, S. Chakraborty, R. Dey, P. K. Panigrahi, I. Meglinski, and N. Ghosh, "Submicron scale tissue multifractal anisotropy in polarized laser light scattering," Laser Phys. Lett. **15**(3), 035601 (2018).

59. W. F. Cheong, S. A. Prahl, and A. J. Welch, "A review of the optical properties of biological tissues," IEEE J. Quantum Electron. **26**(12), 2166–2185 (1990).

60. S. L. Jacques, "Optical properties of biological tissues: a review," Phys. Med. Biol. **58**(11), R37–R61 (2013).

61. T. J. Allen, P. C. Beard, A. Hall, A. P. Dhillon, and J. S. Owen, "Spectroscopic photoacoustic imaging of lipid-rich plaques in the human aorta in the 740 to 1400 nm wavelength range," J. Biomed. Opt. **17**(6), 061209 (2012).

62. J. Xia, A. Weaver, D. E. Gerrard, and G. Yao, "Monitoring sarcomere structure changes in whole muscle using diffuse light reflectance," J. Biomed. Opt. **11**(4), 040504 (2006).

63. H. He, N. Zeng, R. Liao, T. Yun, W. Li, Y. He, and H. Ma, "Application of sphere-cylinder scattering model to skeletal muscle," Opt. Express **18**(14), 15104–15112 (2010).

64. S. Karpf and B. Jalali, "Frequency-doubled FDML-MOPA laser in the visible," Opt. Lett. **44**(24), 5913–5916 (2019).